

ARTICLE

Open Access

# Pressure-induced superconductivity in the nonsymmorphic topological insulator KHgAs

Guangyang Dai<sup>1,2</sup>, Yating Jia<sup>1</sup>, Bo Gao<sup>3</sup>, Yi Peng<sup>1,4</sup>, Jianfa Zhao<sup>1</sup>, Yanming Ma<sup>3</sup>, Changfeng Chen<sup>5</sup>, Jinlong Zhu<sup>1,2</sup>, Quan Li<sup>3</sup>, Runze Yu<sup>1,6</sup> and Changqing Jin<sup>1,4,7</sup>

## Abstract

Recently, topological insulators (TIs) KHgX (X = As, Sb, Bi) with hourglass-shaped dispersion have attracted great interest. Different from the TIs protected by either time-reversal or mirror crystal symmorphic symmetry tested in previous experiments, these materials were proposed as the first material class whose band topology relies on nonsymmorphic symmetries. As a result, KHgX shows many exotic properties, such as hourglass-shaped electronic channels and three-dimensional doubled quantum spin Hall effects. To date, high-pressure experimental studies on these nonsymmorphic TIs are minimal. Here, we carried out high-pressure electrical measurements up to 55 GPa, together with high-pressure X-ray diffraction measurements and high-pressure structure prediction on KHgAs. We found a pressure-induced semiconductor-metal transition between ~16 and 20 GPa, followed by the appearance of superconductivity with a  $T_c$  of ~3.5 K at approximately 21 GPa. The superconducting transition temperature was enhanced to a maximum of ~6.6 K at 31.8 GPa and then slowly decreased until 55 GPa. Furthermore, three high-pressure phases within 55 GPa were observed, and their crystal structures were established. Our results showed the high-pressure phase diagram of KHgAs and determined the pressure-induced superconductivity in nonsymmorphic TIs. Thus, our study can be used to facilitate further research on superconductivity and topologically nontrivial features protected by nonsymmorphic symmetries.

## Introduction

The investigation of topological materials, including topological insulators (TIs), topological semimetals, and topological superconductors, has attracted tremendous interest over the past few decades<sup>1–19</sup>. These topological materials possess exotic fermions (such as Dirac fermions, Weyl fermions, and Majorana fermions) and fascinating physical properties. Therefore, they have potential applications in both spintronics and quantum computation. TIs have a bulk band gap similar to ordinary insulators but exhibit gapless boundary states protected by time-

reversal symmetry. In the last decade, the topological configuration of the electronic states of the system has become increasingly rich by the consideration of additional symmetries<sup>20–22</sup>. Among them, crystal symmetries have played an important role in topological classification, such as crystal point group symmetries, leading to the concept of topological crystalline insulators (TCIs)<sup>23–25</sup>. Recently, by studying spatial symmetries that translated the origin by a fraction of the lattice period, Wang et al. predicted that nonsymmorphic symmetries could protect a novel surface fermion with dispersion shapes similar to an hourglass, and they also proposed KHgX (X = As, Sb, Bi) as a material class to achieve this new hourglass-shaped dispersion<sup>26</sup>. Different from the previously discovered TIs protected by either time-reversal or mirror crystal symmorphic symmetry, the band topology of KHgX relied on nonsymmorphic symmetries. Subsequently, angle-resolved photoemission spectroscopy measurements provided experimental evidence of

Correspondence: Jinlong Zhu (zhujl@sustech.edu.cn) or Quan Li (liquan777@jlu.edu.cn) or Runze Yu (yurz@iphy.ac.cn) or Changqing Jin (Jin@iphy.ac.cn)

<sup>1</sup>Beijing National Laboratory for Condensed Matter Physics, Institute of Physics, Chinese Academy of Sciences, 100190 Beijing, China

<sup>2</sup>Department of Physics, Southern University of Science and Technology, Shenzhen 518055, China

Full list of author information is available at the end of the article

These authors contributed equally: Guangyang Dai, Yating Jia, Bo Gao, Yi Peng

© The Author(s) 2023



**Open Access** This article is licensed under a Creative Commons Attribution 4.0 International License, which permits use, sharing, adaptation, distribution and reproduction in any medium or format, as long as you give appropriate credit to the original author(s) and the source, provide a link to the Creative Commons license, and indicate if changes were made. The images or other third party material in this article are included in the article's Creative Commons license, unless indicated otherwise in a credit line to the material. If material is not included in the article's Creative Commons license and your intended use is not permitted by statutory regulation or exceeds the permitted use, you will need to obtain permission directly from the copyright holder. To view a copy of this license, visit <http://creativecommons.org/licenses/by/4.0/>.

hourglass fermions on the (010) surface of crystalline KHgSb<sup>27,28</sup>.

Usually, topological materials show superconductivity under pressure or by carrier doping<sup>29–36</sup>, which is considered a possible way to achieve topological superconductivity. However, identifying their topological superconductivity is still a difficult task and under debate<sup>35</sup>. In most cases, the transition from TIs to superconductors is accompanied by the crystal and/or electronic structural transition<sup>30,33</sup>. It remains unclear whether this transition is indeed necessary to induce superconductivity in TIs. Therefore, searching for superconductivity in new TIs and identifying the possibility of topological superconductors is still an open question.

In this work, we grew single crystals and conducted a comprehensive study on the electrical transport properties and structural phase transition under high pressure for the nonsymmorphic topological insulator KHgAs. We observed transformations from a semiconductor to a metallic state then to a superconducting state as the pressure increased. High-pressure X-ray diffraction measurements combined with crystal structure prediction indicated that the structure changed from the  $P6_3/mmc$  structure at ambient pressure into  $Pnma$ , then to  $P6_3mc$ , and finally changed to a new  $P6_3/mmc$  structure at pressures of 2.1 GPa, 21.5 GPa, and 26.7 GPa, respectively.

## Results and discussion

### Physical characterization under ambient pressure

The crystal structure of KHgAs is shown in Fig. 1a. It belongs to the hexagonal crystal structure with the space group of  $P6_3/mmc(194)$ <sup>37</sup>. The Hg-As planar honeycomb layers and K ion layers stack alternately along the  $c$  axis, and the K ion is located at an inversion center between the two adjacent Hg-As layers. The obtained crystals were flake-like, and the crystal size could reach  $1\text{ mm} \times 0.8\text{ mm} \times 0.1\text{ mm}$  (see inset of Fig. 1b). Figure 1b shows the X-ray diffraction pattern of the as-grown KHgAs crystals. Only (001) reflections were observed, indicating that the crystals were well oriented along the  $c$  axis. A Le Bail fit to the diffraction data yielded a  $c$  value of  $9.9855\text{ \AA}$ , which coincided with a previous result<sup>37</sup>. The chemical composition of the as-grown single crystals was measured by energy-dispersive X-ray spectroscopy (EDX), as shown in Fig. 1c. The atomic ratio of K:Hg:As was determined to be 1.03(99):1.00:0.94(18), which is close to the ideal stoichiometric formula of KHgAs. The scanning electron microscope image of a KHgAs single crystal is shown in the inset of Fig. 1c. Figure 1d shows the temperature-dependent electrical resistivity of the KHgAs single crystal under ambient pressure. The overall behavior of resistivity displayed a typical semiconducting-like feature, except for a slight resistivity anomaly at approximately 125 K. A similar anomaly was also

observed in the three-dimensional topological material  $\text{ZrTe}_5$ <sup>38</sup> and Rashba semiconductor  $\text{BiTeCl}$ <sup>39</sup>, which was attributed to the possible Lifshitz transition or charge density wave behavior, though its origin still remains controversial<sup>38–40</sup>. According to the thermal activation model, the resistivity  $\rho$  is proportional to  $\exp(\Delta_g/2k_B T)$ , where  $\Delta_g$  is the semiconducting band gap and  $k_B$  is Boltzmann's constant. Hence, the curve of  $\ln(\rho)$  versus  $1/T$  is plotted in the inset of Fig. 1d. The curve could be effectively fitted, and the band gap  $\Delta_g$  of KHgAs was evaluated to be  $\sim 143\text{ meV}$ .

### High-pressure transport properties

Figure 2 shows the high-pressure electrical transport measurements for the KHgAs single crystal. Below 10.3 GPa, the sample maintains semiconductor activity, and the resistances gradually increase with pressure (see Fig. 2a). The anomalous behavior of resistance is gradually suppressed, and the anomalous temperature is reduced to approximately 74 K at 10.3 GPa. From 10.3 GPa to 12.2 GPa, there is a greater increase in resistance at low temperature, which indicates that the sample becomes more insulating. The anomalous behavior of the resistance basically disappears at 12.2 GPa. However, a large resistance anomaly at approximately 90 K reappears at 14.2 GPa, as shown in Fig. 2b. With further increasing pressure, the anomaly peak shifts toward higher temperatures, accompanied by the appearance of metallic transport behavior at low temperature. The phenomenon of anomalies being initially suppressed and then enhanced at low pressure has also been observed in the topological material  $\text{HfTe}_5$ <sup>41</sup>. At 20 GPa, the anomaly peak disappears, and the R-T curve shows metallic behavior over the whole temperature range.

Additionally, a pressure-induced superconducting transition is observed, as shown in Fig. 2c. The transition temperature of onset ( $T_c^{\text{onset}}$ ) is approximately 3.5 K at 21 GPa, which is defined based on the differential of resistance over temperature ( $dR/dT$ )<sup>31</sup>; see the inset of Fig. 2d. Under further compression,  $T_c^{\text{onset}}$  rapidly grows, and a zero-resistance state is observed at 28.7 GPa. Subsequently,  $T_c^{\text{onset}}$  reaches a maximum of approximately 6.6 K at 31.8 GPa, followed by a slow decline with a further increase in pressure.

Figure 2f shows the temperature dependence of resistance under various external magnetic fields along the  $c$ -axis of the KHgAs single crystal at 27.8 GPa. The transition temperature  $T_c^{\text{onset}}$  is gradually suppressed as the magnetic field increases, which provides strong evidence that the transition is superconducting in nature. According to the Werthamer-Helfand-Hohenberg (WHH) formula<sup>42</sup>,  $H_{c2}(0) = -0.691[dH_{c2}(T)/dT]_{T=T_c} * T_c$ , the upper critical field  $H_{c2}(0)$  is determined to be 5.0 T. The Pauli-limiting upper critical field estimated via

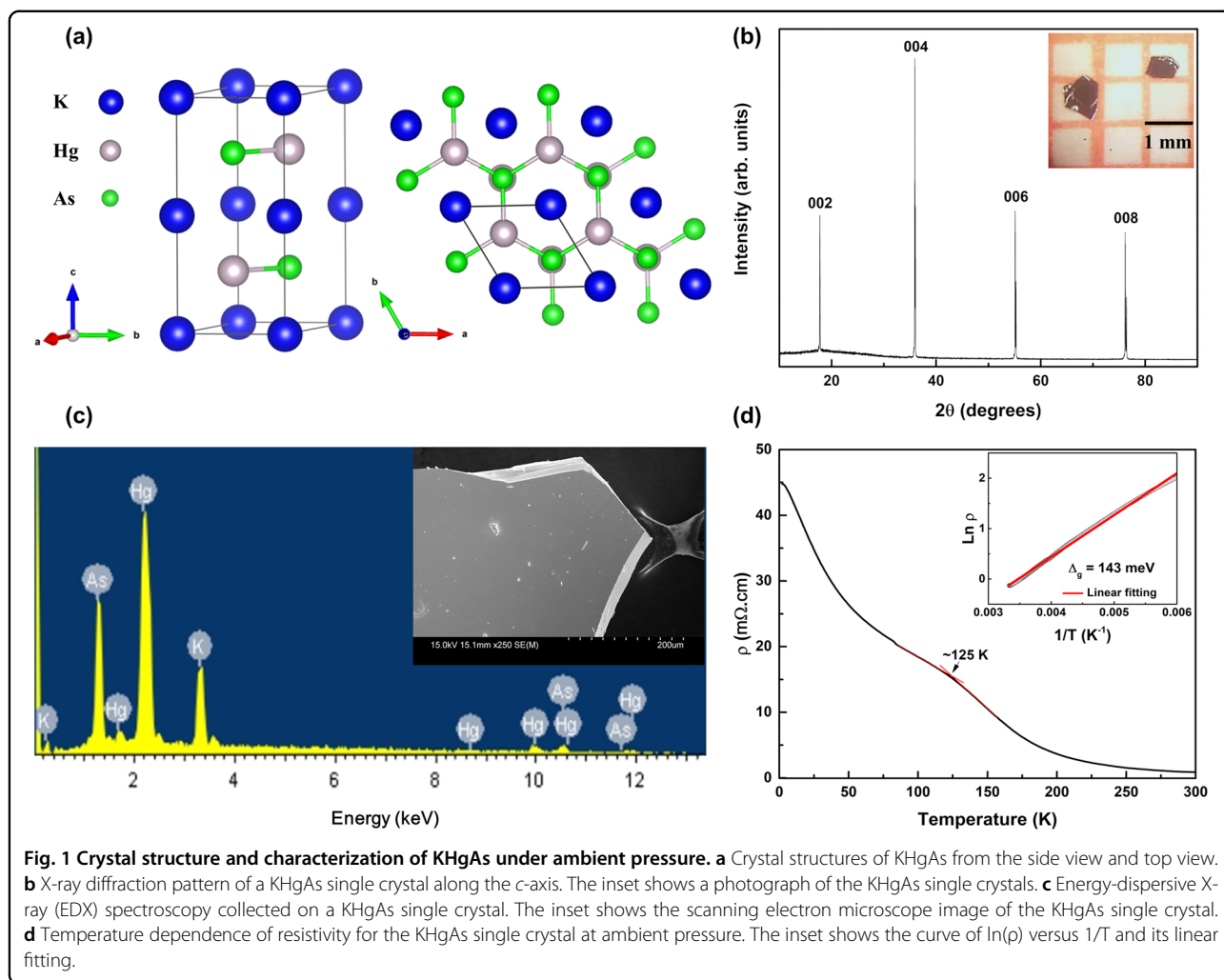


**Fig. 1** Crystal structure and characterization of KHgAs under ambient pressure. **a** Crystal structures of KHgAs from the side view and top view. **b** X-ray diffraction pattern of a KHgAs single crystal along the *c*-axis. The inset shows a photograph of the KHgAs single crystals. **c** Energy-dispersive X-ray (EDX) spectroscopy collected on a KHgAs single crystal. The inset shows the scanning electron microscope image of the KHgAs single crystal. **d** Temperature dependence of resistivity for the KHgAs single crystal at ambient pressure. The inset shows the curve of  $\ln(\rho)$  versus  $1/T$  and its linear fitting.

$H_p(0) = 1.84T_c$  is approximately 9.6 T, far exceeding the measured  $H_{c2}(0)$ , indicating that the spin paramagnetic effect can be neglected.

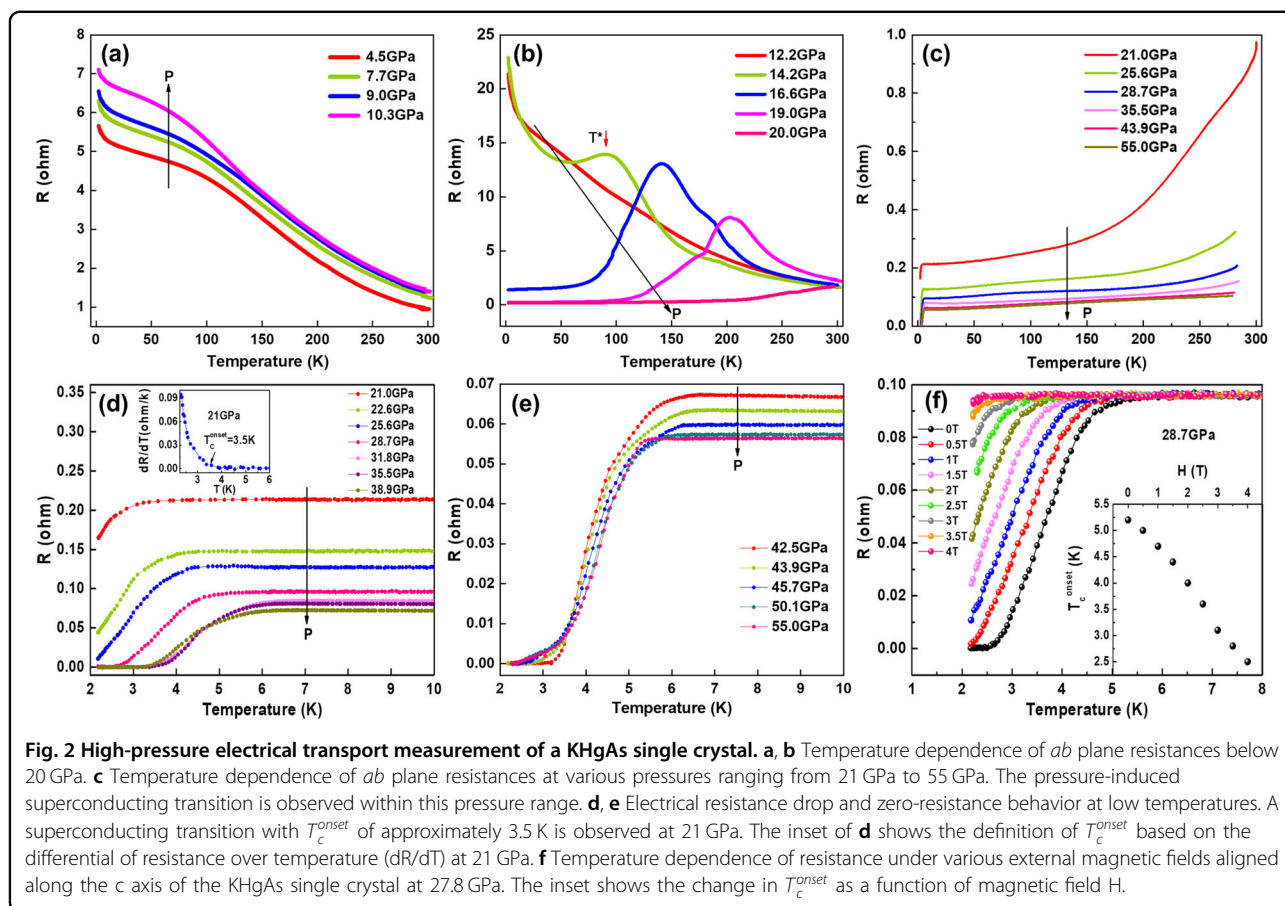
### High-pressure synchrotron X-ray diffraction

Next, we focus on the crystal structure evolution under pressure. X-ray diffraction patterns of KHgAs polycrystalline powder at various pressures are shown in Fig. 3. Below 2.1 GPa, all peaks are effectively indexed as a  $P6_3/mmc$  phase (phase I). Then, a set of new diffraction peaks appear at 2.1 GPa, 3.1 GPa, and 4.8 GPa, which are marked with inverted triangles, rhombi, and asterisks, respectively (see Fig. 3a). By carefully analyzing the diffraction data, we preliminarily conclude that these new peaks all belong to the first high-pressure phase (phase II). Phase I coexists with phase II in the pressure range of 2.1–4.8 GPa, and then the diffraction peaks of phase I almost disappear. When the pressure further increases to 21.5 GPa, two new diffraction peaks marked with arrows appear (see Fig. 3b), which indicates the appearance of

another new high-pressure phase (phase III). Upon further increasing the pressure to 26.7 GPa, the third high-pressure phase (phase IV) appears and gradually becomes the main phase up to 55.1 GPa (see Fig. 3b). Moreover, phase II and phase III still exist until 55.1 GPa.

### High-pressure structure prediction

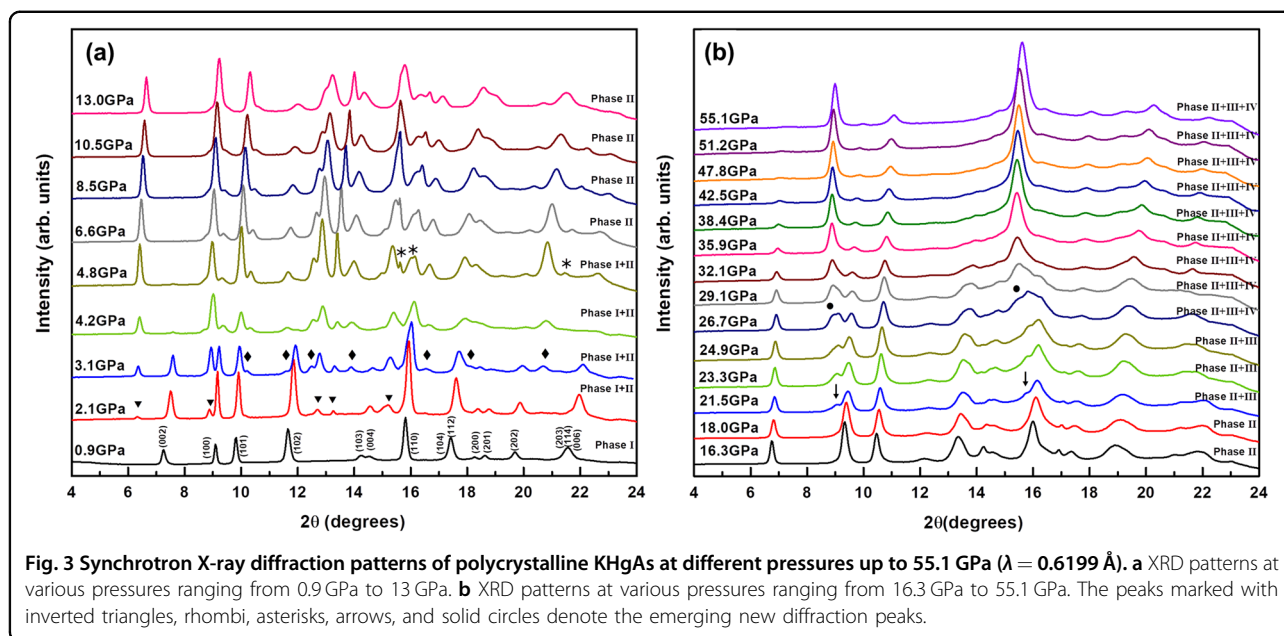
Structure prediction based on the CALYPSO methodology was performed to obtain a deep understanding of the crystal structure evolution of KHgAs under pressure. Figure 4a shows the calculated enthalpy curves of low-energy structures. Below 3.0 GPa, the most stable phase possesses  $P6_3/mmc$  symmetry (Fig. 4b). Then, it undergoes a series of structural evolutions from  $P6_3/mmc$  to  $Pnma$  (Fig. 4c),  $C2/m$  (Fig. 4d),  $P6_3mc$  (Fig. 4e), and finally to a new  $P6_3/mmc$  phase (named  $P6_3/mmc$ -II, Fig. 4f). Upon a thorough examination of the high-pressure XRD pattern, the sample possesses a hexagonal structure as the ambient phase below 2.1 GPa (see Supplementary Fig. S1a in the Supplementary Information). The first high-pressure



phase (phase II, appears at 2.1 GPa) is indexed as a *Pnma* phase. Almost all peaks of the predicted *Pnma* phase can be effectively fitted with the experimental pattern at 10.5 GPa except for an unknown peak at approximately 13 degrees (see Supplementary Fig. S1b in the Supplementary Information). The origin of this peak is discussed in the following section. The XRD patterns between 21.5 GPa and 26.7 GPa can be effectively fitted using the combination of structures of *Pnma* and *P6<sub>3</sub>mc* (except for an additional peak similar to the case at 10.5 GPa, see Supplementary Fig. S1c in the Supplementary Information), rather than the predicted *C2/m* phase. Notably, there are Hg-Hg and As-As bonds in the HgAs layers in the *C2/m* structure (see the right panel of Fig. 4d). These layers are distinctly different from the HgAs layers in the other stable structures, where Hg and As are arranged alternatively. Therefore, a large energy barrier may need to be overcome in the structural transition from *Pnma* to the *C2/m* phase. This is the potential reason that there is no appearance of the *C2/m* phase. Finally, the XRD patterns of KHgAs above 26.7 GPa are fitted with the phases *Pnma* + *P6<sub>3</sub>mc* + *P6<sub>3</sub>/mmc-II* (see Supplementary Fig. S1d in the Supplementary Information). The evolutions of unit cell volumes vs. pressure for different phases are illustrated in

Supplementary Fig. S2 in the Supplementary Information. The unit cell volumes of all phases monotonically decrease with increasing pressure.

To explore the unknown peak of the XRD pattern at 10.5 GPa that cannot be indexed using the predicted *Pnma* structure under hydrostatic pressure conditions, we then investigated the evolution of the structural parameter and XRD pattern with changing external non-hydrostatic stress along typical high symmetric crystal directions. This kind of stress usually exists in ultrahigh-pressure experiments induced by nonideal transmitting media and can effectively modulate the interatomic distances and bonding patterns. Here, we investigated the evolution of XRD patterns for the *Pnma* structure at 10.5 GPa with changing external stress along the typical [001], [110], and [111] crystal directions. The applied strain effectively modulated the interatomic distances and bonding patterns, e.g., peak shifting, splitting, and broadening. When the tensile strain increased from 0% to 5%, the simulated theoretical XRD data along the [001] tensile strain showed excellent agreement with the experimental patterns, especially for the unknown peak position near 13 degrees, as shown in Supplementary Fig. S3a in the Supplementary Information. Similarly, the XRD



pattern at 23.3 GPa could also be excellently fitted by the introduction of 5% tensile strain along the [001] deformation direction (Supplementary Fig. S3b).

#### Temperature–pressure phase diagram

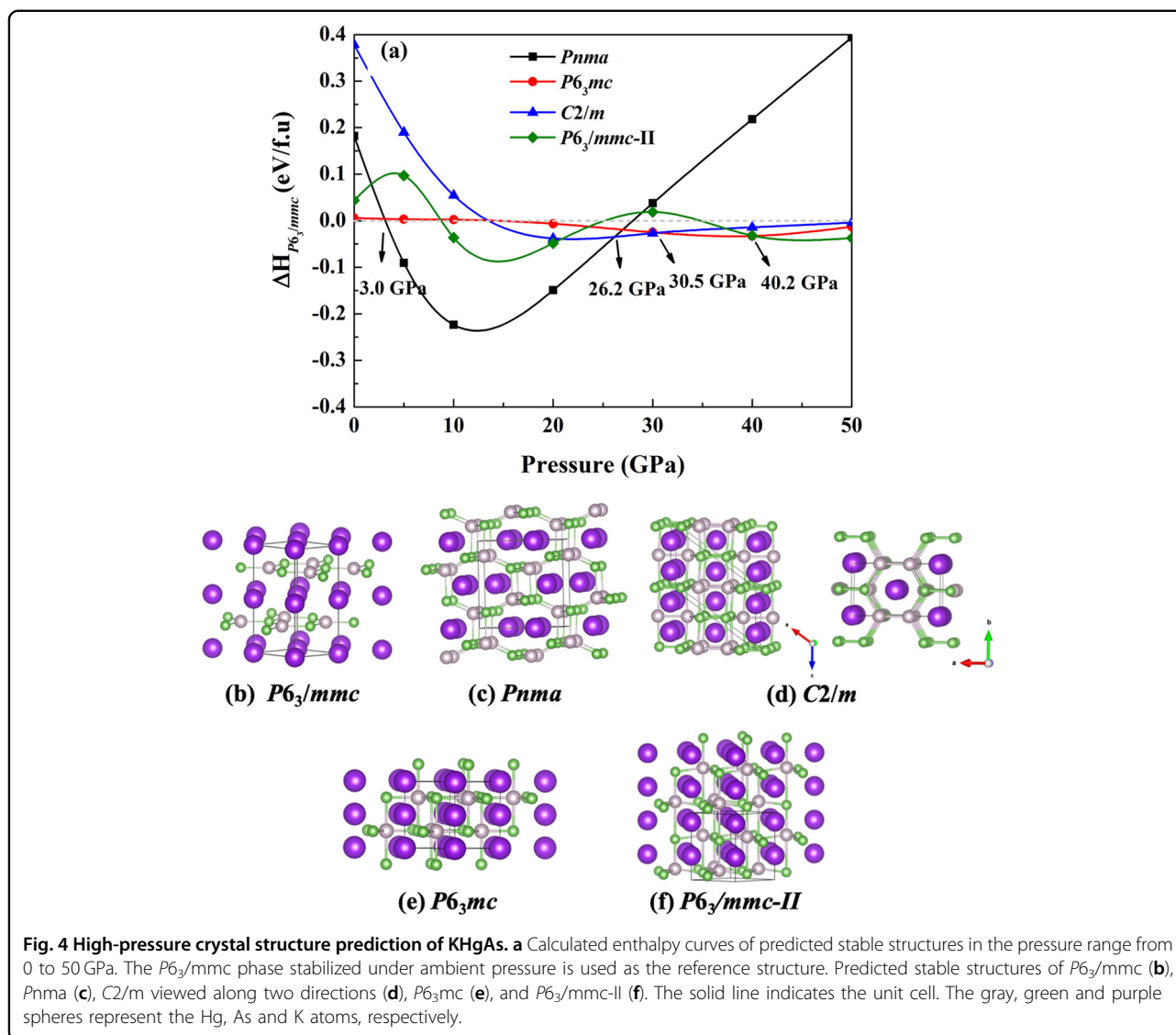
Based on the results of electrical transport measurements, structure prediction, and structure refinement at high pressures, the phase diagram of KHgAs as a function of pressure is obtained, as shown in Fig. 5. Below 12.2 GPa, KHgAs shows semiconductor activity. The anomalous temperature is reduced from  $\sim 125$  K at ambient pressure to  $\sim 74$  K at 10.3 GPa and basically disappears at 12.2 GPa. Then, a large resistance anomaly at approximately 90 K reappears at 14.2 GPa, and the temperature of the anomaly peak increases to 200 K with increasing pressure, accompanied by the appearance of metallic transport behavior at low temperature. At 20 GPa, the anomaly peak disappears, and the R-T curve shows metallic behavior over the whole temperature range. Then, a clear superconducting transition with  $T_c^{\text{onset}}$  of  $\sim 3.5$  K appears at 21 GPa. The  $T_c^{\text{onset}}$  is enhanced to a maximum value of  $\sim 6.6$  K at 31.8 GPa and then is slowly suppressed under further compression. Finally, a dome-shaped pressure dependence of  $T_c^{\text{onset}}$  is obtained.

For the structural change under pressure, KHgAs maintains the ambient structure below 2.1 GPa with  $P6_3/mmc$  and then shifts to a new orthorhombic structure with space group  $Pnma$  under pressure. This phase exists over almost the entire pressure range. A new phase with space Group  $P6_3mc$  appears at approximately 21.5 GPa. Notably, the superconducting transition also appears at

approximately 21 GPa, this result indicates that there may be some intrinsic connection between superconductivity and the  $P6_3mc$  phase, which warrants in-depth study. Both the  $Pnma$  and  $P6_3mc$  phases exist under heavy compression but with the appearance of a new  $P6_3/mmc$ -II phase at approximately 26.7 GPa.

#### Conclusion

In summary, we successfully grew high-quality single crystals of the newly developed nonsymmorphic topological insulator KHgAs and examined the pressure effect below 55 GPa. Our electrical transport measurement showed a semiconductor-metal transition between  $\sim 16$  and 20 GPa, and finally, pressure-induced superconductivity with a  $T_c^{\text{onset}}$  of  $\sim 3.5$  K was successfully observed at 21 GPa.  $T_c^{\text{onset}}$  was enhanced to a maximum value of  $\sim 6.6$  K as the pressure increased to 31.8 GPa and then was slowly suppressed under further compression. High-pressure X-ray diffraction combined with crystal structure prediction indicated that the structure changed from the  $P6_3/mmc$  structure at ambient pressure into a new orthorhombic structure with space group  $Pnma$  at 2.1 GPa, then changed to the  $P6_3mc$  structure at 21.5 GPa, and finally changed to the  $P6_3/mmc$ -II structure at approximately 26.7 GPa. Moreover, nonhydrostatic stress played an important role in the high-pressure behavior of KHgAs. Our results showed the possible coexistence of superconductivity and a topologically nontrivial feature protected by nonsymmorphic symmetries and could potentially provide a new platform to investigate the interplay between topological properties and superconductivity. However, detailed band structure



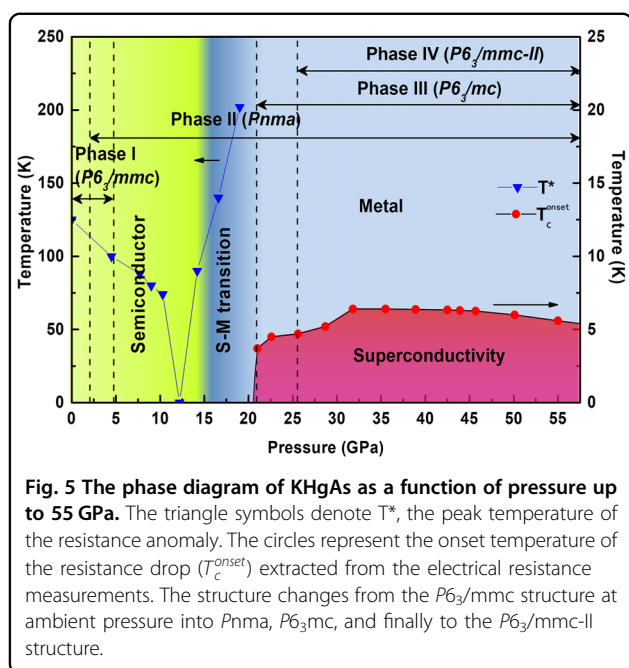
calculations for the high-pressure phase of KHgAs are needed to provide definitive evidence.

## Materials and methods

### Sample preparation and characterization

Single crystals of KHgAs were grown using the melting method. To grow single crystals, we first prepared polycrystalline samples of KHgAs. High-purity K (99.95%) and As (99.999%) were mixed at a molar ratio of 1:1, sealed into a titanium tube filled with high-purity Ar gas, and heated to 500 °C to prepare the precursor KAs. Then, the mixtures of KAs and Hg in a molar ratio of 1:1 were placed into an  $Al_2O_3$  capsule and sealed into a titanium tube filled with high-purity Ar gas. The mixture was heated to 500 °C and held for 20 h before cooling to room temperature. Finally, the obtained polycrystalline samples were sealed into a niobium tube and then an evacuated

quartz tube. The quartz tube was heated to 900 °C at a rate of 4 °C/min and maintained at this temperature for 10 h. Then, the sample was slowly cooled to 500 °C at a rate of 3 °C/h. To protect the samples from reacting with air or water, all the synthesis processes were carried out in a high-purity Ar atmosphere. X-ray diffraction (XRD) at ambient pressure was performed on a Rigaku Ultima VI (3KW) diffractometer using Cu  $K\alpha$  radiation generated at 40 kV and 40 mA. The chemical composition of the as-grown single crystals was measured by energy-dispersive X-ray spectroscopy (EDX) using a spectrometer (Model EDAX GENESIS XM2 SYSTEM 60x) equipped with a field-emission scanning electron microscope (Hitachi S-4800). The electrical resistivity under ambient pressure was measured on a Quantum Design physical property measurement system (PPMS) using the four-probe method.



### High-pressure electric transport measurement

The electronic transport properties of KHgAs single crystals under high pressure and low temperatures were investigated via the four-probe electrical conductivity method in a diamond anvil cell (DAC) made of CuBe alloy as described in refs. <sup>31,43</sup>. The pressure was generated by a pair of diamonds with a 100  $\mu\text{m}$  diameter culet. A gasket made of T301 stainless steel was pressed from a thickness of 250  $\mu\text{m}$  to 10  $\mu\text{m}$ , and a center hole with a diameter of 120  $\mu\text{m}$  was drilled. Fine cubic boron nitride (c-BN) powder was used to cover the gasket to protect the electrode leads insulated from the metallic gasket. The electrodes were slim Au wires with a diameter of 18  $\mu\text{m}$ . A 50- $\mu\text{m}$ -diameter center hole in the insulating layer served as the sample chamber. The dimensions of the sample were approximately 35  $\mu\text{m} \times 35 \mu\text{m} \times 5 \mu\text{m}$ , and NaCl powder was used as the pressure transmitting medium. The pressure was measured via the ruby fluorescence method at room temperature before and after each cooling<sup>44</sup>. A diamond anvil cell was placed inside a MagLab system to perform the experiments. The temperature was automatically controlled by a program of the MagLab system. A thermometer was mounted near the diamond in the diamond anvil cell to monitor the exact sample temperature.

### High-pressure ADXRD experiments

In situ high-pressure angle-dispersive X-ray diffraction (ADXRD) experiments were performed using a symmetric Mao Bell DAC at the Beijing Synchrotron Radiation Facility. The X-ray wavelength was 0.6199  $\text{\AA}$ . The sample in the DAC was a finely grounded polycrystalline powder,

and ruby balls were placed near the sample as pressure markers. The two-dimensional image plate patterns were converted to one-dimensional  $2\theta$  versus intensity data using the Fit2d software package<sup>45</sup>. The high-pressure synchrotron X-ray diffraction patterns were refined by the Rietveld method<sup>46</sup> through the GSAS program.

### Crystal structure prediction

The structure prediction was performed using the swarm-intelligence-based CALYPSO method<sup>47,48</sup>, which is a leading structure prediction method and can be used to search multidimensional PESs in an unbiased manner. The structural searches were carried out with simulation cell sizes of 2, 4, 6, and 8 formula units at 5, 22, 30, and 50 GPa. The density functional theory framework as implemented in the Vienna Ab Initio simulation package (VASP)<sup>49</sup> was used for the structure optimization and total energy evaluation. The projector-augmented wave method<sup>50</sup> is adopted, and  $3p^6 4s^1$ ,  $5d^{10} 6s^2$ , and  $4s^2 4p^3$  are used as the valence electrons for K, Hg, and As, respectively. The generalized gradient approximation of Perdew, Burke, and Ernzerhof<sup>51</sup> was selected for the exchange-correlation functional. The plane-wave kinetic energy cutoff of 500 eV and a Monkhorst–Pack K-spacing of  $2\pi \times 0.025 \text{\AA}^{-1}$  in reciprocal space were chosen to ensure that the total energy converged to less than 1 meV/atom.

### Acknowledgements

This work was supported by the National Science Foundation and Ministry of Science and Technology of China through research projects (2022YFA1403800, 2018YFA0305700, 11921004, U2032220, T2325013, 52288102, 52090024, 12034009) and the Beijing Nature Science Foundation (2202059).

### Author details

<sup>1</sup>Beijing National Laboratory for Condensed Matter Physics, Institute of Physics, Chinese Academy of Sciences, 100190 Beijing, China. <sup>2</sup>Department of Physics, Southern University of Science and Technology, Shenzhen 518055, China. <sup>3</sup>State Key Lab of Superhard Materials and Key Laboratory of Material Simulation Methods & Software of Ministry of Education, College of Physics, Jilin University, Changchun 130012, China. <sup>4</sup>School of Physical Sciences, University of Chinese Academy of Sciences, 100190 Beijing, China. <sup>5</sup>Department of Physics and Astronomy, University of Nevada, Las Vegas, NV 89154, USA. <sup>6</sup>Center for High Pressure Science and Technology Advanced Research (HPSTAR), 100094 Beijing, China. <sup>7</sup>Songshan Lake Materials Laboratory, Dongguan 523808, China

### Author contributions

C.Q.J. designed the experiments. G.Y.D., Y.P. and J.F.Z. synthesized the KHgAs single crystals and performed the physical characterization under ambient pressure. G.Y.D. performed the high-pressure synchrotron radiation X-ray experiments. Y.T.J. carried out the high-pressure resistivity measurements. B.G., Y.M.M., C.F.C. and Q.L. contributed to the crystal structure prediction. G.Y.D., B.G. and Q.L. analyzed the experimental data and plotted the figures with input from all other authors. G.Y.D., R.Z.Y., Q.L. and J.L.Z. wrote the manuscript. All authors participated in discussions and comments on the paper.

### Conflict of interest

The authors declare no competing interests.

### Publisher's note

Springer Nature remains neutral with regard to jurisdictional claims in published maps and institutional affiliations.

**Supplementary information** The online version contains supplementary material available at <https://doi.org/10.1038/s41427-023-00496-7>.

Received: 11 January 2022 Revised: 20 July 2023 Accepted: 1 August 2023.  
Published online: 6 October 2023

## References

- Bernevig, B. A., Hughes, T. L. & Zhang, S. C. Quantum spin Hall effect and topological phase transition in HgTe quantum wells. *Science* **314**, 1757–1761 (2006).
- Hsieh, D. et al. A topological Dirac insulator in a quantum spin Hall phase. *Nature* **452**, 970–974 (2008).
- Zhang, H. J. et al. Topological insulators in Bi<sub>2</sub>Se<sub>3</sub>, Bi<sub>2</sub>Te<sub>3</sub> and Sb<sub>2</sub>Te<sub>3</sub> with a single Dirac cone on the surface. *Nat. Phys.* **5**, 438–442 (2009).
- Chen, Y. L. et al. Experimental realization of a three-dimensional topological insulator, Bi<sub>2</sub>Te<sub>3</sub>. *Science* **325**, 178–181 (2009).
- Qi, X. L. & Zhang, S. C. The quantum spin Hall effect and topological insulators. *Phys. Today* **63**, 33–38 (2010).
- Hasan, M. Z. & Kane, C. L. Colloquium: topological insulators. *Rev. Mod. Phys.* **82**, 3045–3067 (2010).
- Qi, X. L. & Zhang, S. C. Topological insulators and superconductors. *Rev. Mod. Phys.* **83**, 1057 (2011).
- Wan, X. G., Turner, A. M., Vishwanath, A. & Savrasov, S. Y. Topological semimetal and Fermi-arc surface states in the electronic structure of pyrochlore iridates. *Phys. Rev. B* **83**, 205101 (2011).
- Wang, Z. et al. Dirac semimetal and topological phase transitions in A<sub>3</sub>Bi (A=Na, K, Rb). *Phys. Rev. B* **85**, 195320 (2012).
- Wang, Z. J., Weng, H. M., Wu, Q. S., Dai, X. & Fang, Z. Three-dimensional Dirac semimetal and quantum transport in Cd<sub>3</sub>As<sub>2</sub>. *Phys. Rev. B* **88**, 125427 (2013).
- Liu, Z. K. et al. Discovery of a three-dimensional topological Dirac semimetal, Na<sub>3</sub>Bi. *Science* **343**, 864–867 (2014).
- Neupane, M. et al. Observation of a three-dimensional topological Dirac semimetal phase in high-mobility Cd<sub>3</sub>As<sub>2</sub>. *Nat. Commun.* **5**, 3786 (2014).
- Weng, H. M., Fang, C., Fang, Z., Bernevig, B. A. & Dai, X. Weyl semimetal phase in noncentrosymmetric transition-metal monophosphides. *Phys. Rev. X* **5**, 011029 (2015).
- Huang, S. M. et al. A Weyl Fermion semimetal with surface Fermi arcs in the transition metal monophenitide TaAs class. *Nat. Commun.* **6**, 7373 (2015).
- Soluyanov, A. A. et al. Type-II Weyl semimetals. *Nature* **527**, 495–498 (2015).
- Qi, X. L., Hughes, T. L., Raghu, S. & Zhang, S. C. Time-reversal-invariant topological superconductors and superfluids in two and three dimensions. *Phys. Rev. Lett.* **102**, 187001 (2009).
- Fu, L. & Kane, C. L. Superconducting proximity effect and Majorana fermions at the surface of a topological insulator. *Phys. Rev. Lett.* **100**, 096407 (2008).
- Akhmerov, A. R., Nilsson, J. & Beenakker, C. W. J. Electrically detected interferometry of majorana fermions in a topological insulator. *Phys. Rev. Lett.* **102**, 216404 (2009).
- Ryu, S., Schnyder, A. P., Furusaki, A. & Ludwig, A. W. W. Topological insulators and superconductors: tenfold way and dimensional hierarchy. *N. J. Phys.* **12**, 065010 (2010).
- Schnyder, A. P., Ryu, S., Furusaki, A. & Ludwig, A. W. W. Classification of topological insulators and superconductors in three spatial dimensions. *Phys. Rev. B* **78**, 195125 (2008).
- Mong, R. S. K., Essin, A. M. & Moore, J. E. Antiferromagnetic topological insulators. *Phys. Rev. B* **81**, 245209 (2010).
- Li, R. D., Wang, J., Qi, X. L. & Zhang, S. C. Dynamical axion field in topological magnetic insulators. *Nat. Phys.* **6**, 284–288 (2010).
- Fu, L. A. Topological crystalline insulators. *Phys. Rev. Lett.* **106**, 106802 (2011).
- Hsieh, T. H. et al. Topological crystalline insulators in the SnTe material class. *Nat. Commun.* **3**, 982 (2012).
- Tanaka, Y. et al. Experimental realization of a topological crystalline insulator in SnTe. *Nat. Phys.* **8**, 800–803 (2012).
- Wang, Z. J., Alexandradinata, A., Cava, R. J. & Bernevig, B. A. Hourglass fermions. *Nature* **532**, 189–194 (2016).
- Ma, J. Z. et al. Experimental evidence of hourglass fermion in the candidate nonsymmorphic topological insulator KHgSb. *Sci. Adv.* **3**, e1602415 (2017).
- Liang, A. J. et al. Observation of the topological surface state in the nonsymmorphic topological insulator KHgSb. *Phys. Rev. B* **96**, 165143 (2017).
- Ilina, M. A. & Itskovich, E. S. Superconductivity of bismuth telluride at high-pressure. *Fiz. Tverd. Tela* **17**, 154–157 (1975).
- Einaga, M. et al. New superconducting phase of Bi<sub>2</sub>Te<sub>3</sub> under pressure above 11 GPa. *J. Phys. Conf. Ser.* **215**, 012036 (2010).
- Zhang, J. L. et al. Pressure-induced superconductivity in topological parent compound Bi<sub>2</sub>Te<sub>3</sub>. *Proc. Natl Acad. Sci. USA* **108**, 24–28 (2011).
- Matsubayashi, K., Terai, T., Zhou, J. S. & Uwatoko, Y. Superconductivity in the topological insulator Bi<sub>2</sub>Te<sub>3</sub> under hydrostatic pressure. *Phys. Rev. B* **90**, 125126 (2014).
- Kirshenbaum, K. et al. Pressure-induced unconventional superconducting phase in the topological insulator Bi<sub>2</sub>Se<sub>3</sub>. *Phys. Rev. Lett.* **111**, 087001 (2013).
- Zhu, J. et al. Superconductivity in topological insulator Sb<sub>2</sub>Te<sub>3</sub> induced by pressure. *Sci. Rep.* **3**, 2016 (2013).
- Hor, Y. S. et al. Superconductivity in Cu<sub>x</sub>Bi<sub>2</sub>Se<sub>3</sub> and its implications for pairing in the undoped topological insulator. *Phys. Rev. Lett.* **104**, 057001 (2010).
- Sharma, M. M., Sharma, P., Karn, N. K. & Awana, V. P. S. Comprehensive review on topological superconducting materials and interfaces. *Supercon. Sci. Technol.* **35**, 083003 (2022).
- Vogel, R. & Schuster, H. U. KHgAs(Sb) and KZnAs - ternary compounds in a modified Ni<sub>2</sub>In-structure. *Z. Naturforsch. B Chem. Sci.* **35**, 114–116 (1980).
- Zhou, Y. H. et al. Pressure-induced superconductivity in a three-dimensional topological material ZrTe<sub>5</sub>. *Proc. Natl Acad. Sci. USA* **113**, 2904 (2016).
- Ying, J. J. et al. Realization of insulating state and superconductivity in the Rashba semiconductor BiTeCl. *Phys. Rev. B* **93**, 100504 (2016).
- Zhang, Y. et al. Electronic evidence of temperature-induced Lifshitz transition and topological nature in ZrTe<sub>5</sub>. *Nat. Commun.* **8**, 15512 (2017).
- Liu, Y. et al. Superconductivity in HfTe<sub>5</sub> across weak to strong topological insulator transition induced via pressures. *Sci. Rep.* **7**, 44367 (2017).
- Werthamer, N. R., Helfand, E. & Hohenberg, P. C. Temperature and purity dependence of superconducting critical field, H<sub>c2</sub>. III. Electron spin and spin-orbit effects. *Phys. Rev.* **147**, 295 (1966).
- Zhang, S. J. et al. The comprehensive phase evolution for Bi<sub>2</sub>Te<sub>3</sub> topological compound as function of pressure. *J. Appl. Phys.* **111**, 112630 (2012).
- Mao, H. K., Xu, J. & Bell, P. M. Calibration of the ruby pressure gauge to 800 Kbar under quasi-hydrostatic conditions. *J. Geophys. Res. Solid* **91**, 4673–4676 (1986).
- Hammersley, A. P., Svensson, S. O., Hanfland, M., Fitch, A. N. & Hausermann, D. Two-dimensional detector software: from real detector to idealised image or two-theta scan. *High. Press. Res.* **14**, 235–248 (1996).
- Toby, B. H. EXPGUI, a graphical user interface for GSAS. *J. Appl. Crystallogr.* **34**, 210–213 (2001).
- Wang, Y. C., Lv, J. A., Zhu, L. & Ma, Y. M. Crystal structure prediction via particle-swarm optimization. *Phys. Rev. B* **82**, 094116 (2010).
- Wang, Y. C., Lv, J., Zhu, L. & Ma, Y. M. CALYPSO: a method for crystal structure prediction. *Comput. Phys. Commun.* **183**, 2063–2070 (2012).
- Kresse, G. & Joubert, D. From ultrasoft pseudopotentials to the projector augmented-wave method. *Phys. Rev. B* **59**, 1758–1775 (1999).
- Bloch, P. E. Projector augmented-wave method. *Phys. Rev. B* **50**, 17953–17979 (1994).
- Perdew, J. P., Burke, K. & Ernzerhof, M. Generalized gradient approximation made simple. *Phys. Rev. Lett.* **77**, 3865–3868 (1996).